

Thermal Chameleon: Task-Adaptive Tone-mapping for Radiometric Thermal-Infrared images

Dong-Guw Lee¹, Jeongyun Kim¹, Younggun Cho², and Ayoung Kim^{1*}

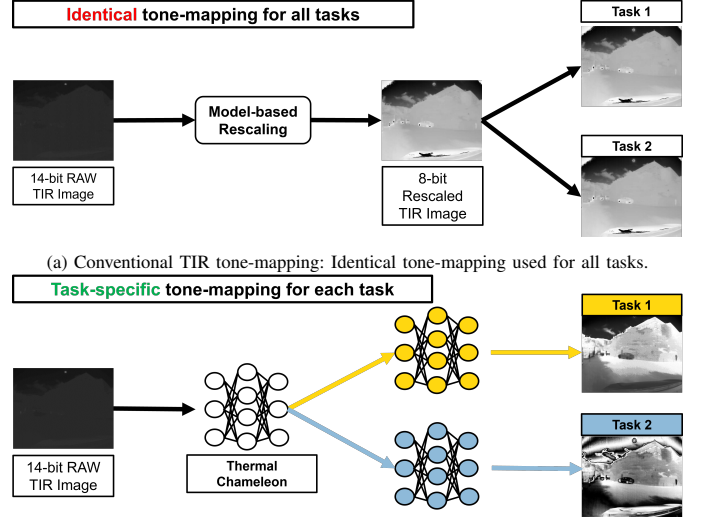
Abstract—Thermal Infrared (TIR) imaging provides robust perception for navigating in challenging outdoor environments but faces issues with poor texture and low image contrast due to its 14/16-bit format. Conventional methods utilize various tone-mapping methods to enhance contrast and photometric consistency of TIR images, however, the choice of tone-mapping is largely dependent on knowing the task and temperature dependent priors to work well. In this paper, we present Thermal Chameleon Network (TCNet), a task-adaptive tone-mapping approach for RAW 14-bit TIR images. Given the same image, TCNet tone-maps different representations of TIR images tailored for each specific task, eliminating the heuristic image rescaling preprocessing and reliance on the extensive prior knowledge of the scene temperature or task-specific characteristics. TCNet exhibits improved generalization performance across object detection and monocular depth estimation, with minimal computational overhead and modular integration to existing architectures for various tasks. Project Page: <https://github.com/donkeymouse/ThermalChameleon>

Index Terms—Thermal Imaging, Robot perception

I. INTRODUCTION

Thermal infrared (TIR) images operate in the long wave infrared spectrum, perceiving the environment through temperature. This characteristic ensures robust perception in adverse environments with poor illumination and airborne obscurants, making TIR sensors desirable for robotics [1] and computer vision [2]. However, since TIR images are usually stored in 14 or 16-bit format, such high dynamic range results in narrow image distribution, yielding ambiguous object boundaries and poor image contrasts [3].

A common way to address such issue is by linearly rescaling TIR images with their minimum and maximum pixel values, however, this method performs poorly on long tailed image distribution caused by hot or cold objects [4]. Recent works have proposed improved tone-mapping methods to maintain photometric consistency between consecutive frames [2, 5] or



(a) Conventional TIR tone-mapping: Identical tone-mapping used for all tasks. (b) Thermal Chameleon Net is a learning-based network that task-adaptively tonemaps TIR images optimized for each task.

Fig. 1: (a): Conventional methods use a single TIR representation for all tasks (b): TCNet is a learning-based tone-mapping network for TIR images. Given the same network, TCNet achieves different tone-mapping, tailored for each task.

use non-linear gains to enhance contrast [6, 7, 8]. Nonetheless, as shown in Fig. 1a, existing methods apply identical tone-mapping for all TIR images. Thus, users must rely on extensive domain knowledge and heuristics to select the appropriate tone-mapping for a given task, requiring excessive handcrafting and familiarity with the temperature data.

In this work, we propose Thermal Chameleon Network (TCNet), a task-adaptive tone-mapping network for radiometric TIR images. Inspired by [9], which replaced conventional image processing with neural network-based tone-mapping for raw RGB images, TCNet similarly replaces model-based rescaling with neural network-based tone-mapping (Fig. 1b). This approach achieves task-optimized tone-mapping, eliminating extensive preprocessing. Unlike recent learning-based TIR tasks that rely on preprocessing a single identical TIR image, TCNet integrates tone mapping within the network to produce different representations of the same TIR image optimized for each task. This eliminates the need for users to know task-specific characteristics or scene temperature priors for choosing the adequate tone-mapping method.

Our contributions are summarized as follows:

- **Temperature-aware data representation and augmentation:** We propose thermal embedding, a data augmentation technique for radiometric TIR images. Thermal embedding uses absolute per-pixel temperature as a com-

Manuscript received: July, 31, 2024; October, 7, 2024.

This paper was recommended for publication by Editor Markus Vincze upon evaluation of the Associate Editor and Reviewers' comments. This work was jointly supported by the New Faculty Startup Fund from Seoul National University, the Korea Agency for Infrastructure Technology Advancement (KAIA) grant funded by the Ministry of Land, Infrastructure and Transport (Grant RS-2023-00250727) through the Korea Floating Infrastructure Research Center at Seoul National University, and the National Research Foundation of Korea(NRF) grant funded by the Korea government(MSIT) (No. RS-2023-00302589)

¹D. Lee, J. Kim, and A. Kim are with the Department of Mechanical Engineering, SNU, Seoul, S. Korea [donkeymouse, jeongyunkim, ayoungk]@snu.ac.kr

²Y. Cho is with the Department of Electrical Engineering, Inha University, Incheon, S. Korea yg.cho@inha.ac.kr

Digital Object Identifier (DOI): see top of this page.

mon ground to create multiple TIR representations from a single image. This simulates varying environmental temperatures without requiring extensive knowledge of the environment, improving the ability to represent high dynamic range TIR images. This enhances data diversity, particularly for monocular image-based tasks.

- **Adaptive Channel Compression:** TCNet employs an adaptive channel compression to assign task-specific weights to each thermal embedding. This facilitates task-adaptive tone-mapping, promotes modular integration into various tasks, and reduces computational overhead and artifacts.
- **Task-adaptive tone-mapping:** TCNet formulates task-optimized tone-mapping for different tasks, eliminating the need for excessive preprocessing and domain knowledge to select optimal tone-mapping for unseen environment. Additionally, task-adaptive tone mapping provides insights into the image characteristics favored by each task.

II. RELATED WORK

A. TIR image tone-mapping

Tone-mapping in TIR images, also known as image rescaling, usually refer to the process of converting raw 14-bit TIR images into 8-bit format. Such process can be categorized into linear and non-linear rescaling. For linear rescaling, previous works estimate adequate maximum and minimum rescaling parameters through TIR camera models [5], temporal windows [10], or clipping bounds established at the 1st and 99th percentile of the image distribution [2].

Non-linear rescaling enhances local and global contrasts of TIR images. Shin et al. [7] employed variable bin-based CLAHE to standardize long-tailed distributions in TIR images. JointTMO [8] used multiscale Retinex transform with a tone-mapping network, but the performance of the learning-based tone-mapping is upper-bounded by the quality of the ground truths tone-mapped image used for training. Fieldscale [6] proposed 2D grid-based min and max rescaling, however, temporal coherence between frame is not preserved. Overall, non-linear rescaling methods tend to attenuate local details within the less populated regions of the image and amplifies the noise inherent to TIR images.

While most tasks focus on improving image preprocessing aspects of TIR images, thereby yielding a single image representation for all tasks, we introduce the first task-dependent, learning-based tone-mapping network for TIR images, allowing for self-optimized tone-mapping tailored to specific tasks.

B. Advances in TIR Image Augmentation

Traditional RGB-based tone-mapping applies variants of gamma correction to Bayer-filtered RGB images. However, these methods are designed for multiple luminance channels and are not suitable for TIR images, which operate on a single luminance channel [8]. Previous works have used image inversion [11] to diversify TIR images, but since then, only few advancements to TIR image-based augmentation have emerged.

Learning-based methods use neural networks to estimate gamma correction parameters or refine images [9]. However, these methods often rely on Bayer filtering to standardize a single high dynamic range image into multiple representations, which is not feasible for TIR images. Thermal embedding addresses this gap by representing a single raw high dynamic range TIR image into multiple representations, facilitating learning-based tone-mapping for TIR images.

C. TIR image-based robotics applications

RAW TIR images have been prominently used in direct SLAM methods [1, 4] for their ability to retain photometric consistency. Ensuring this consistency between pairs of TIR images is crucial for low-level vision tasks such as monocular depth estimation [10, 7, 2] and pose estimation [12]. However, due to low contrast in the TIR images, many methods rely on supervision from other sensors such as LiDAR [1] or RGB images [12]. For object detection, non-linear rescaling is often used to maximize global contrast, though it can lead to image saturation [6, 13].

Choosing the right rescaling method depends on the environmental context of the scene. Histogram equalization is commonly used for TIR images with long-tailed distributions [7], while linear scaling is preferred for tasks requiring temporal consistency. Ultimately, optimal results demand extensive domain knowledge of the scene and task from the users.

TCNet optimizes TIR image processing independently, without the need for auxiliary supervision from other modalities. It uses task-dependent losses to create task-optimized TIR images, eliminating the ambiguity of choosing the right tone mapping. Additionally, the adaptive channel compression module allows for integration into various existing architectures, supporting multiple downstream tasks.

III. METHOD

A. Overview

An overview of TCNet is depicted in Fig. 2. TCNet comprises two stages: multichannel thermal embedding and adaptive channel compression. First, multichannel thermal embedding encodes a single-channel RAW TIR image into multiple thermal embeddings, concatenated channel-wise (green). Then, adaptive channel compression extracts weights from each thermal embedding to compute task-adaptive tone-mapping, forming a three-channel tone-mapped feature (blue). Finally, this feature is propagated into the downstream task.

B. Multichannel Thermal Embedding

1) *Absolute temperature conversion:* Different TIR cameras have varying offsets and lens calibration parameters, leading to discrepancies in encoded pixel values. These differences cause distribution shifts due to temperature variations and camera model discrepancies. To address this, we convert 14-bit RAW TIR images into absolute temperatures in degrees Celsius using formula driven from Planck's Law [14]. This

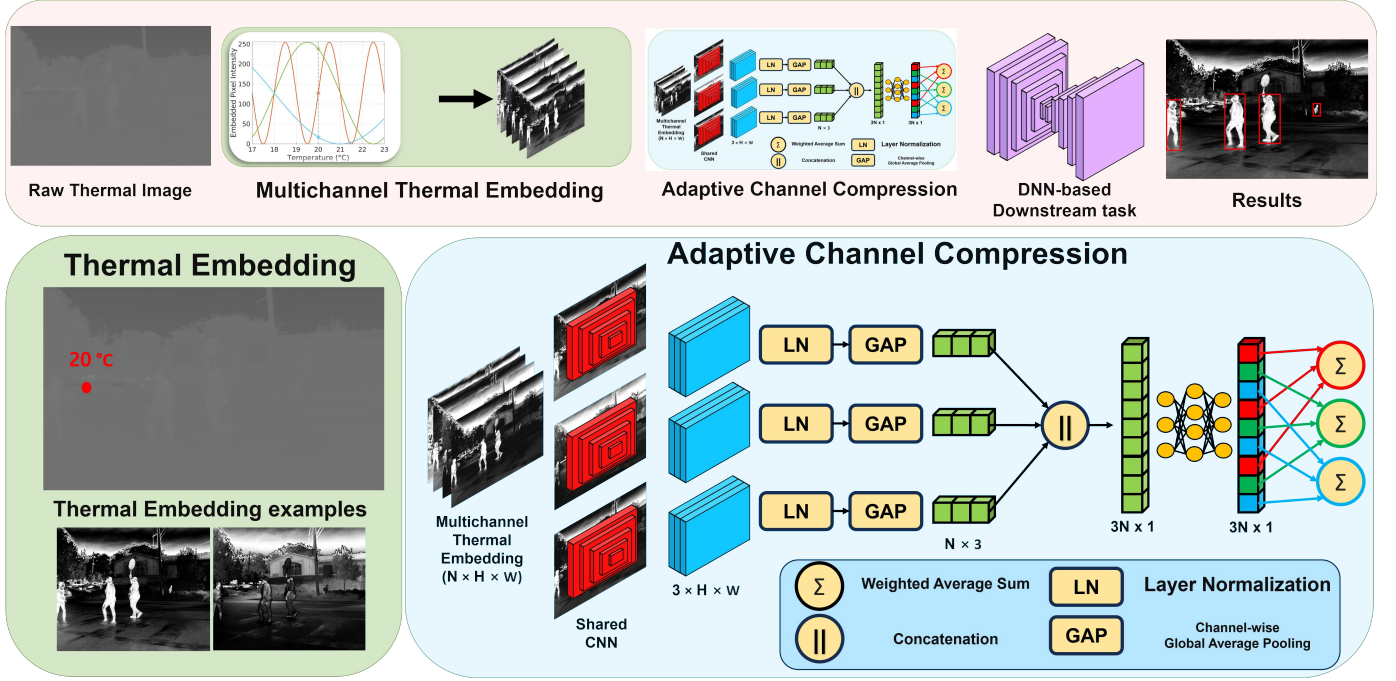


Fig. 2: Overview of Thermal Chameleon Network. The network consists of two stages: multichannel thermal embedding (green) which formulates diverse representations from a 14-bit radiometric TIR images and an adaptive channel compression network (blue) that adaptively compresses these multichannel thermal embeddings into 3 channels which is then used to be trained on downstream tasks. All components are trained in an end-to-end manner.

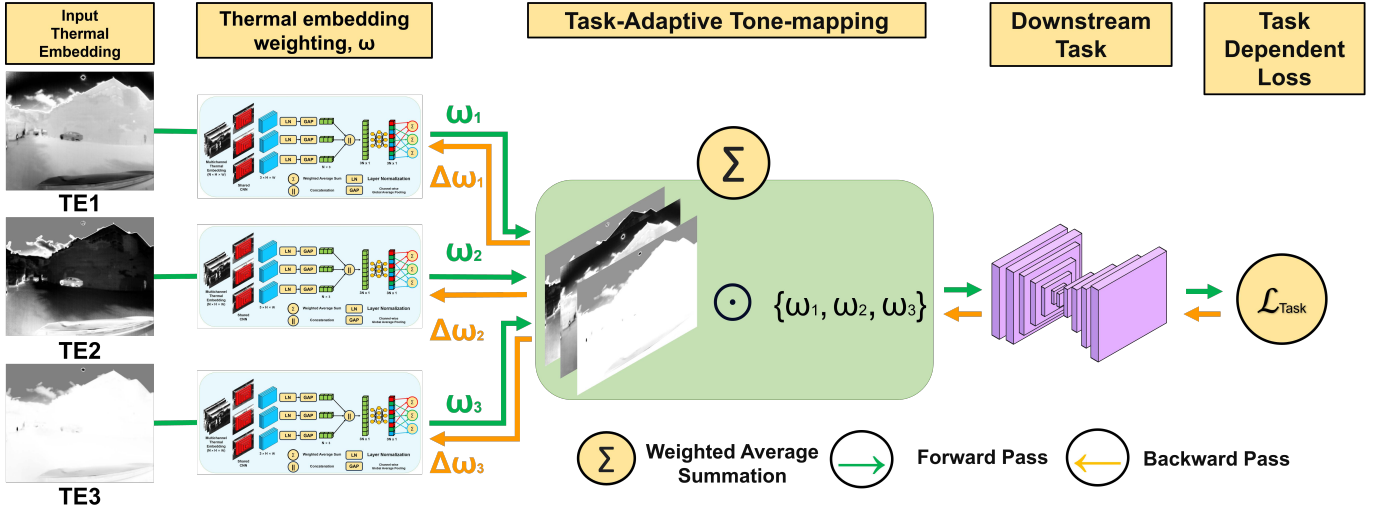


Fig. 3: Adaptive channel compression. Given multichannel TIR embedding, the network assigns adaptive weightings for each thermal embedding optimized by the task-dependent loss. Using such weightings, we adaptively tone-map TIR images via weighted average summation of each thermal embedding and the respective weights.

standardization ensures a consistent representation of temperature across different cameras.

$$I_C = \frac{P}{\ln\left(\frac{R}{S-O} + F\right)} - 273.15 \quad (1)$$

where P and R are constants derived from speed of light, the Boltzmann constant, and Planck's constant, S is the value of the 14-bit RAW TIR image pixel, O and F are the TIR camera's offset and calibration parameters.

2) *Thermal embedding*: Thermal embedding projects a temperature image I_C using a sinusoidal embedding $I_{ME} : \mathbb{R}^{B \times H \times W \times 1} \times \mathbb{N}^{1 \times N} \mapsto \mathbb{R}^{B \times H \times W \times N}$, as denoted by Equation (2)

$$I_{ME} = \big\|_{i=1}^N \left(\frac{255}{2} \cdot \sin\left(\frac{I_C}{D_i} \cdot \pi\right) + \frac{255}{2} \right) \quad (2)$$

where D , B , N , H , W and $\|$ symbolize a set of temperature periodic constants, batch size, number of channels, image height, image width, and channel-wise concatenation of thermal embeddings respectively. Here, $D = \{D_1, D_2, \dots, D_N\}$ in which each D is used to map a single temperature to different intensities. We apply thermal embedding (2) with randomly selected D_i to form a N -channel thermal embedding.

The idea of sinusoidal function for embedding temperature is inspired from [15], which embeds a single RAW RGB

image into multiple representations based on the rolling shutter speed. Since rolling shutter speed is not applicable to RAW TIR images, we use the temperature periodic constant D to simulate a similar effect.

Varying D controls the appearance of the thermal embedding: smaller D values create sharp edges with artifacts, while larger D values can saturate the image. Selecting D values does not require extensive prior knowledge of the environment, but an approximate range. We find that randomly sampling D values between 4.5 and 45 adapts well to various outdoor environments.

3) *Intuition behind thermal embedding*: A 14-bit RAW TIR pixel value spans a much wider range than 8-bit tone-mapped images, making it difficult to represent small temperature differences. Multichannel thermal embedding uses multiple sinusoidal functions to map temperatures to different intensities, allowing higher resolution representation of small temperature differences. This method simulates TIR images from diverse environments and provides a detailed, temperature-aware representation of 14-bit RAW TIR images.

C. Adaptive channel compression

A critical aspect of thermal embedding involves determining the optimal temperature period D to ensure effective representation of the given TIR image for the downstream task. While employing multiple channels can enrich feature representation, not all multichannel embeddings yield beneficial results; some may introduce artifacts and degrade performance. Thus, relying solely on multichannel thermal embedding requires prior knowledge to estimate the optimal D for the task.

However, adaptive channel compression eliminates the need to estimate D values by applying task-specific tone-mapping weights to each thermal embedding, as shown in Fig. 3. Consider a multichannel thermal embedding, $I_{ME} \in \mathbb{R}^{B \times N \times H \times W}$. With temperature periods sampled from a uniform distribution, each embedding passes through shared CNN with two strided convolutional layers and ReLU activation. The extracted features form a 3-channel feature map, resulting in an output shape of $B \times N \times 3 \times H \times W$.

Unlike direct channel concatenation in [9], this method applies layer normalization followed by a global average pooling to each channel, yielding $N \times 3$ feature vectors for each thermal embedding. To encode adaptive weights, these vectors are concatenated and passed through multilayer perceptron (MLP) layers with two 64 hidden units and a single layer with $3N$ layer. The output, activated by Softmax, forms task-adaptive weights for each thermal embedding. Ultimately, each weighted embedding is tone-mapped into a single 3-channel image through per-channel weighted summation, as shown in Equation 3.

$$\mathbf{X}'_i = \sum_{n=1}^N \omega_{\text{norm},i}[n] \cdot I_{ME,n} \quad \text{for } i \in \{1, 2, 3\} \quad (3)$$

where ω refers to channel weightings for the compressed channel index i and $I_{ME,n}$ refers to the n th thermal embedding. Finally, the compressed input is then passed as a 3-channel input to the downstream task network.

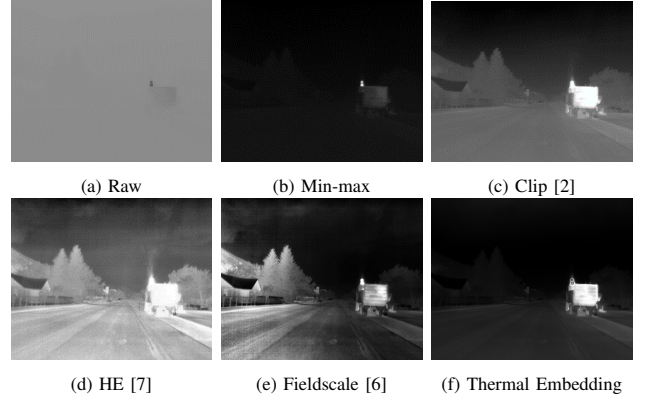


Fig. 4: Visualization examples of commonly used baseline TIR tone-mapping methods. D value of 3 is used for thermal embedding

TABLE I: Dataset overview

Dataset	Mean Temperature $^{\circ}\text{C}$	S.t.d Temperature $^{\circ}\text{C}$	Location	Scene	# of images
FLIR-ADAS v2 - Train	18.00	14.30	USA (California), England, France	Urban	10,724
FLIR-ADAS v2 - Test	18.49	15.04	USA: California, Idaho, Michigan	Urban, Sub-urban	2,151
STheReO - Valley (Test)	26.34	8.12	Korea: Daejeon	Sub-urban	955
VIVID - Outdoor Day (Train)	15.03	12.67	Korea: Daejeon	Campus	2,213
VIVID - Outdoor Night (Test)	15.57	7.90	Korea: Daejeon	Campus	2,019
MS2 - Test	30.70	2.77	Korea: Daejeon	Campus, Urban, Resident	22,919

IV. EXPERIMENTS

A. Experiment Overview

We evaluate the performance of TCNet on two popular downstream tasks: object detection and monocular depth estimation. In addition, we analyze the task adaptive characteristic of TCNet based on its intermediate tone-mapped images for each downstream task.

1) *Datasets*: Table I presents an overview of the datasets used in our experiments. To use TCNet, the TIR image must be stored in its RAW format by a radiometric TIR camera with known camera offset parameters. As a result, only tasks that fulfill this requirement are object detection and self-supervised depth estimation. For each task, we used the FLIR-ADAS v2 [16] dataset for object detection and VIVID [17] benchmark for depth estimation. We further assessed zero-shot performance on unseen datasets with significant temperature and geographical variations. For object detection, we manually annotated the valley sequence from the STheReO [18] dataset based on classes overlapping with the FLIR dataset. For depth estimation, we selected the MS2 dataset [19] test sequence. For all evaluations, TCNet was trained exclusively on the training set and subsequently tested various test sets.

2) *Baselines*: We used different 14-bit to 8-bit TIR image rescaling methods as the baseline models. Tone-mapped visualizations of the baselines are shown in Fig. 4. Descriptions to the baseline tone-mapping methods are shown below:

- RAW: Linear rescaling with $2^{14} - 1$ (max resolution)
- Min-max: Linear rescaling with min/max value

TABLE II: Quantitative detection results on FLIR ADAS [16]. Best results highlighted in **bold**; Second best in underlines.

Dataset	FLIR ADAS						
Model	Baseline	mAP	mAP @0.5	mAP @0.75	mAP @small	mAP @medium	mAP @large
RetinaNet	FLIR AGC	25.2	49.8	22.5	14.7	49.4	58.4
	Clip [2]	24.1	45.8	22.9	12.1	50.9	60.0
	HE [7]	23.4	46.0	21.0	11.8	48.9	60.6
	Min-max	22.3	49.2	15.9	12.7	44.5	51.6
	RAW	20.1	37.4	19.1	6.1	45.8	58.5
	FieldScale [6]	20.6	49.8	23.9	14.5	52.3	57.7
	TE(3)	<u>29.1</u>	<u>50.8</u>	<u>28.7</u>	<u>15.9</u>	<u>59.4</u>	<u>64.2</u>
	TE(10)	28.6	50.0	27.8	15.4	57.1	64.2
	TCNet	34.7	53.3	37.4	22.7	64.1	67.7
YOLO-X	FLIR AGC	53.5	81.4	57.6	<u>45.8</u>	70.0	71.5
	Clip [2]	49.1	75.4	52.9	42.1	65.6	58.9
	HE [7]	40.7	64.9	41.8	31.4	63.4	64.5
	Min-max	50.8	81.6	53.9	43.1	67.5	71.7
	RAW	37.9	63.3	39.5	27.1	62.2	62.1
	FieldScale [6]	<u>54.0</u>	<u>82.2</u>	<u>59.8</u>	47.8	<u>73.0</u>	<u>75.8</u>
	TE(3)	53.3	80.9	58.2	44.8	72.0	73.9
	TE(10)	51.1	78.4	54.8	41.5	72.1	76.9
	TCNet	56.0	83.8	60.5	47.8	73.4	77.0
Sparse-RCNN	FLIR AGC	37.5	60.9	41.0	29.2	55.0	63.4
	Clip [2]	38.4	61.8	42.4	30.6	56.7	62.4
	HE [7]	39.1	62.5	43.1	32.2	54.8	61.8
	Min-max	37.9	63.0	39.7	31.1	52.8	58.6
	RAW	12.3	24.9	11.7	7.9	22.8	19.8
	FieldScale [6]	37.2	59.3	40.6	27.9	56.6	66.0
	TE(3)	<u>41.6</u>	<u>65.3</u>	<u>45.0</u>	<u>32.5</u>	<u>61.1</u>	<u>63.7</u>
	TE(10)	26.8	43.9	29.2	19.9	43.3	33.2
	TCNet	45.7	70.5	49.8	36.1	67.5	69.1

- Clip [2]: Locally consistent linear rescaling with 1% and 99% of the image intensity used as the clipping parameters.
- HE [7]: Bin-based histogram equalization used. Bin size of 30 is used.
- Fieldscale [6]: 2D min and max field-based non-linear rescaling. Used provided default parameters.
- TE(N): N channel thermal embedding.

B. Evaluation on object detection

1) *Implementation Details*: We evaluated three object detection architectures: RetinaNet [20], YOLOX [21], and Sparse-RCNN [22], using baselines from a previous work [9]. No changes were made to the downstream models' architectures, except for TCNet, which was integrated into the front end. We uniformly sampled N temperature periods within the 4.5 to 45 range, as periods beyond this range offered no additional benefit.

The detection networks were trained according to their original loss functions, excluding color augmentations and image resizing. Except for Thermal Embedding (TE) and TCNet, all baselines used 3-channel TIR images by repeating the single-channel image to utilize ImageNet initialization, except for YOLOX. Models were trained on 640×512 pixel images, and the detection performance was evaluated using mean average precision (mAP) following standard COCO evaluation protocols.

2) *Evaluation on FLIR*: Table II shows the detection result evaluated on the FLIR-ADAS dataset. As predicted, the direct use of RAW images worsened performance compared to 8-bit rescaled images. In contrast, TCNet outperformed all baselines by 12.4%, 5.2%, and 7.8% for RetinaNet, YOLOX, and Sparse-RCNN respectively. Even using thermal embedding alone (TE(3)) improved performance over the baselines. Adaptive channel compression further enhanced detection performance by 6.1%, 4.9%, and 4.1% for RetinaNet, YOLOX, and

TABLE III: Quantitative detection results on STheReO [18]. Best results highlighted in **bold**; Second best in underlines.

Dataset	STheReO - Valley						
Model	Baseline	mAP	mAP @0.5	mAP @0.75	mAP @small	mAP @medium	mAP @large
RetinaNet	FLIR AGC	-	-	-	-	-	-
	Clip	31.2	57.4	29.9	7.9	40.6	59.9
	HE	29.6	56.8	26.5	6.9	38.7	58.1
	Min-max	20.8	35.6	21.5	5.0	21.2	30.2
	RAW	27.7	54.9	24.4	7.9	35.4	52.4
	FieldScale	21.9	46.7	18.6	5.0	28.1	49.6
	TE(3)	35.4	62.2	35.9	10.0	45.8	62.7
	TE(10)	33.2	<u>61.4</u>	32.5	<u>10.3</u>	42.5	57.5
	TCNet	36.1	62.0	37.3	12.6	46.8	66.6
YOLO-X	FLIR AGC	-	-	-	-	-	-
	Clip	47.0	80.6	47.7	24.7	56.2	73.8
	HE	45.3	76.8	45.5	22.3	54.1	72.8
	Min-max	46.5	82.0	46.2	25.5	55.1	69.9
	RAW	40.9	70.4	41.1	17.0	49.6	64.1
	FieldScale	47.1	79.2	48.4	22.7	<u>57.1</u>	76.8
	TE(3)	46.8	80.4	47.9	24.3	55.8	73.4
	TE(10)	<u>47.5</u>	80.5	49.0	24.3	56.5	75.1
	TCNet	48.3	<u>81.3</u>	50.0	<u>24.9</u>	57.6	<u>76.4</u>
Sparse-RCNN	FLIR AGC	-	-	-	-	-	-
	Clip	22.7	45.4	19.8	10.5	30.3	32.1
	HE	10.7	20	10.1	2.1	14.6	31.1
	Min-max	34.9	64	34.5	15.6	42.4	57.9
	RAW	4.1	9.5	3.7	0.8	5.9	6.5
	FieldScale	31.3	58.3	30.8	13.0	41.0	47.3
	TE(3)	<u>38.3</u>	<u>71.2</u>	<u>37.7</u>	<u>17.3</u>	<u>48.5</u>	69.1
	TE(10)	17.9	37.8	14.1	9.9	23.0	20.0
	TCNet	39.5	73.2	38.2	18.8	49.4	<u>63.5</u>

Sparse-RCNN respectively. However, increasing the number of thermal embeddings without adaptive channel compression reduced performance, likely because detection networks are optimized for 3-channel RGB images.

3) *Zero-shot Evaluation on STheReO*: Table III shows the zero-shot detection results on the STheReO dataset. TCNet also demonstrates the best overall performance over the baseline models, achieving either the best or second best performance in all metrics. We posit such improvement originates from the use of thermal embedding, effectively simulating a temperature-aware data augmentation. This is critical because thermal image datasets are typically small, and they capture a limited range of environments. As a solution, TCNet's thermal embedding diversifies the representation of TIR images, mimicking different environmental temperatures during training. This approach enhances the model's robustness to environmental changes, making TCNet particularly effective in generalizing to unseen data. This compensates for the limited diversity within thermal image datasets and ensuring reliable object detection across diverse temperature conditions.

For advanced models like YOLOX that use extensive geometric augmentation, the performance gap between TCNet and linear scaling methods decreases on the STheReO dataset. This is likely due to the small temperature and scene variations in the test set and the small evaluation size, resulting in fewer image degradation issues. Nonetheless, TCNet combined with geometric augmentation still yields the best detection performance.

C. Evaluation on geometric tasks

1) *Implementation Details*: We evaluated TCNet on two geometric tasks: monocular depth estimation and pose estimation. As for the baseline model, we selected Monodepth2-based TIR depth estimation model from prior research [7], which is a self-supervised model for estimating both depth

TABLE IV: Depth estimation result on VIVID. Best results highlighted in **bold**; Second best in underlines.

Method	Error				Accuracy		
					δ	δ	δ
	AbsRel	SqRel	RMS	RMSlog	1.25	1.25 ²	1.25 ³
Raw	0.633	9.006	11.454	0.597	0.361	0.572	0.717
Minmax	0.552	7.875	10.616	0.539	0.440	0.633	0.767
HE	0.109	<u>0.703</u>	<u>4.132</u>	<u>0.150</u>	0.887	0.98	<u>0.994</u>
Clip	0.132	0.926	5.090	0.182	0.823	0.965	0.99
Fieldscale	0.544	8.158	10.874	0.532	0.453	0.643	0.769
Shin [10]	0.157	1.179	5.802	0.211	0.750	0.948	0.985
Shin [2]	0.111	0.778	4.177	0.153	0.889	0.981	<u>0.994</u>
TE(3)	<u>0.102</u>	0.824	4.198	<u>0.150</u>	<u>0.904</u>	<u>0.984</u>	<u>0.994</u>
TE(10)	0.124	0.863	4.464	0.169	0.851	0.966	0.989
TCNet	0.098	0.611	3.683	0.136	0.915	0.985	0.995

TABLE V: Depth results for MS2 dataset. Best results highlighted in **bold**; Second best in underlines.

Method	Error				Accuracy		
					δ	δ	δ
	AbsRel	SqRel	RMS	RMSlog	1.25	1.25 ²	1.25 ³
Raw	0.477	4.473	11.174	0.654	0.278	0.514	0.72
Minmax	0.784	28.167	17.554	0.742	<u>0.384</u>	0.590	0.704
HE	0.603	9.730	12.322	0.641	0.321	0.619	0.743
Clip	0.395	4.589	10.386	0.584	0.322	0.619	0.796
Fieldscale	0.548	6.142	13.565	0.72	0.225	0.445	0.661
Shin [10]	0.577	11.598	15.031	0.614	0.265	0.53	0.757
TE(3)	0.447	11.442	10.960	<u>0.467</u>	0.298	0.556	0.754
TE(10)	<u>0.342</u>	3.616	<u>10.043</u>	0.488	0.329	<u>0.636</u>	<u>0.836</u>
TCNet	0.335	<u>4.267</u>	9.286	0.462	0.435	0.686	0.837

and pose. During training, we followed the original hyperparameters and loss functions outlined by [7], with an exception to the training epochs which we extended it to 400. All models leveraged ImageNet preinitialization on its backbone. Additionally, we also compare it with multi-spectral [10, 2] models. For evaluation on the MS2 dataset, we only evaluate models whom have open-sourced training code or pre-trained model available. Given that both depth and pose model use a shared encoder, we also use a shared TCNet for both task, training TCNet in a multi-task manner.

2) *Experiment results*: Table IV and Table V presents monocular depth estimation results evaluated on VIVID [17] as well as zero-shot evaluation on the MS2 dataset [19] respectively. TCNet surpasses not only models trained with existing baselines, but also outperforms models trained with multi-spectral data; it especially shows strong generalization performance to unseen environment. Aligning with the previous findings, the use of thermal embedding on the MS2 dataset [19] improves the performance, showcasing its robustness to unseen data despite the difference in the average temperature and type of the scene. Out of the conventional methods, we find that HE and Clip yields the best depth estimation performance on the VIVID and MS2 dataset respectively. Thus, without extensive prior knowledge of the environment, non-optimal performance is achieved. On the contrary, with task-adaptive tone-mapping element, TCNet, is able to achieve consistent performance across diverse environments. For ego-pose estimation, which is the other counterpart, we observe a similar trend; results related to this is further discussed in the supplementary material.

TABLE VI: Task-adaptivity analysis for tone-mapped images

Dataset	Object Detection		Depth Estimation		Tone-mapped Distribution
	Image Entropy	Perceptual Similarity	Image Entropy	Perceptual Similarity	
					KL-Divergence
FLIR-ADAS	2.64	0.75	3.37	0.72	13.70
ViVID++	3.73	0.72	4.03	0.69	12.68
STheReO	3.72	-0.40	3.96	-0.48	15.01

D. Task-adaptivity Analysis

1) *Quantitative evaluation*: Image entropy can be considered as one of the key qualitative metric for determining the contrast of an image. Similarly, high level image characteristics are evaluated by measuring the perceptual similarity of two images using pretrained backbones; notably recent methods has shifted towards using multimodal embedding models trained on large corpus of data such as CLIP [23].

To verify our hypothesis on task-adaptive nature of TCNet, we examine both low and high level image characteristics of tone mapped images. For low level characteristic, we compute the image entropy of the tone mapped image per each task. For high level characteristic, we adopt coarsely paired RGB-TIR evaluation sets from FLIR, STheReO, and VIVID test set to compute the perceptual similarity between coarse image pairs. For this, we leverage ImageBind [24], a large multimodal feature embedding model that supports both RGB and TIR images to compute embedding vector for each daylight RGB and TIR image pairs and measure their cosine similarity.

Table VI shows the characteristics of tone-mapped images for object detection and monocular depth estimation. We observe that tone-mapped images for depth estimation tend to have higher image entropy compared to those for object detection, which yield higher perceptual similarity. For depth estimation, higher entropy means higher contrast in the low-level pixel space, which is crucial for sharp depth near object boundaries. In contrast, object detection relies on feature vectors extracted from deeper layers, requiring high semantic validity and resulting in high perceptual similarity to RGB images despite lower contrast. Notably, the STheReO dataset shows negative perceptual similarity, unlike the other datasets. This result likely stems from the need to resize RGB images for use with the ImageBind.

To further demonstrate the task adaptivity, we visualize the average data distribution of the tone-mapped images from each dataset in Fig. 5. Here, we identify that each task exhibit different tone-mapped distribution, with differing KL-divergence values; thus, demonstrating that TCNet tonemaps different TIR images per different task.

2) *Qualitative evaluation*: Fig. 6 illustrates the tone-mapped visualizations of TCNet for object detection and depth estimation. In both tasks, we observe different characteristics highlighted for each image. For object detection, it focuses on highlighting the thermal characteristics of the objects of interest (green box) while it neglects fine details of the background. Conversely, for depth estimation, it tends to neglect details on the objects within the image, but rather focuses on achieving finer edges and boundaries in the background, which is pivotal for depth estimation.

3) *Artifact rejection*: To verify artifact rejection capability through adaptive channel compression, we analyze the weights

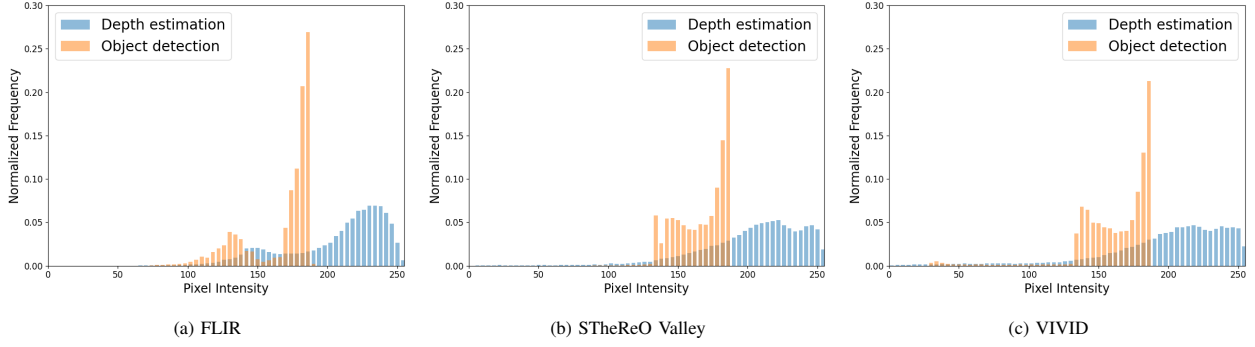


Fig. 5: Average image histogram distribution of the tone-mapped images across different datasets. Different tasks tone-map the same TIR images differently.

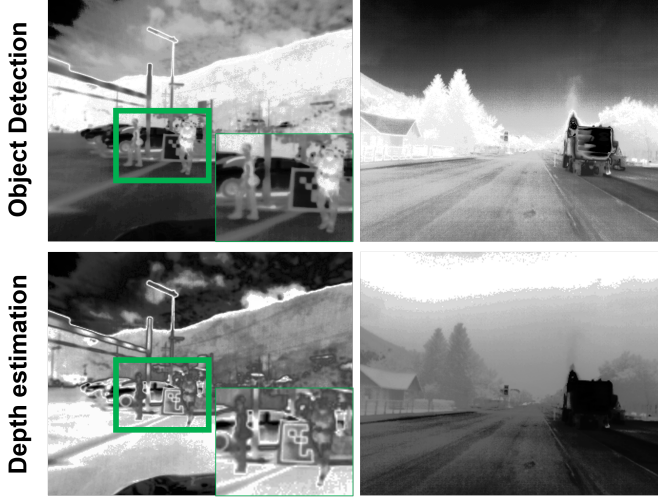


Fig. 6: Example tone-mapped TIR images for object detection and depth estimation. Object detection focuses on preserving object specific characteristics while depth focuses on preserving sharp boundaries between background and objects and neglecting dynamic objects within the scene. See supplementary for more visualizations.

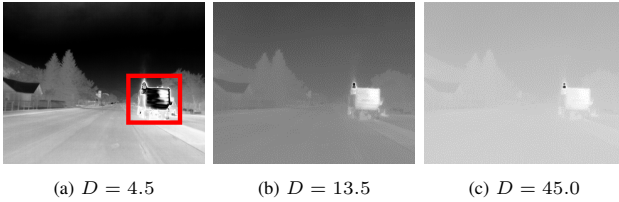


Fig. 7: Thermal embeddings with their respective thermal temperature periods.

assigned for each downstream task. Fig. 7 illustrates the sample thermal embedding used for the task-adaptive tone-mapping, and Table VII shows their respective weightings assigned for each image in the last layer of the adaptive channel compression. Here, we observe a presence of image artifacts in the first thermal embedding (red box). Upon the

TABLE VII: Task adaptive weight visualization

Channels	Thermal Embeddings					
	$D = 4.5$		$D = 13.5$		$D = 45.0$	
	Obj Det	Depth	Obj Det	Depth	Obj Det	Depth
R	0.265	0.108	0.386	0.573	0.349	0.319
G	0.194	0.004	0.236	0.251	0.570	0.745
B	0.137	0.001	0.332	0.788	0.531	0.211
Average	0.199	0.038	0.318	0.537	0.483	0.425

TABLE VIII: Detection results for varying channel sizes

Dataset: FLIR-ADAS						
RetinaNet						
Compression	mAP	mAP @0.5	mAP @0.75	mAP @small	mAP @medium	mAP @large
3 \rightarrow 3	32.5	52.9	35.4	21.2	60.2	55.0
8 \rightarrow 3	33	51.8	35.2	20.0	63.1	67.7
10 \rightarrow 3	34.7	53.3	37.4	22.7	64.1	56.5
12 \rightarrow 3	33.9	51.2	35.6	20.3	62.1	62.1
YOLO-X						
Compression	mAP	mAP @0.5	mAP @0.75	mAP @small	mAP @medium	mAP @large
3 \rightarrow 3	54.8	83.3	58.2	47.0	72.3	72.1
8 \rightarrow 3	55.5	83.0	59.8	47.4	73.2	74.9
10 \rightarrow 3	55.8	82.4	58.4	45.8	72.7	72.9
12 \rightarrow 3	56.0	83.8	60.5	47.8	73.4	77.0
Sparse RCNN						
Compression	mAP	mAP @0.5	mAP @0.75	mAP @small	mAP @medium	mAP @large
3 \rightarrow 3	45	69.8	49.7	36.4	65.3	57.6
8 \rightarrow 3	45.6	69.7	49.0	35.1	69.2	65.7
10 \rightarrow 3	44.8	69.5	49.1	35.1	66.8	66.7
12 \rightarrow 3	45.7	70.5	49.8	36.1	67.5	62.7

presence of such artifacts, we observe that the adaptive channel compression assign lowest weightings for the first thermal embedding for both tasks. However, what we find interesting is that images tone-mapped with object detection tends to be more lenient towards image artifacts than depth estimation, yielding images that retain thermal characteristic of the object. In contrast, depth estimation favors images that highlight the background details while suppressing the details of the objects (green box) that might result in depth uncertainties.

E. Ablation studies

TABLE IX: Depth estimation results for varying channel sizes

Compression	Error				Accuracy		
	AbsRel	SqRel	RMS	RMSlog	δ	$\delta^{1.25^2}$	$\delta^{1.25^3}$
3 \rightarrow 3	0.098	0.611	3.683	0.136	0.915	0.985	0.995
8 \rightarrow 3	0.109	0.725	4.038	0.148	0.976	0.977	0.993
10 \rightarrow 3	0.109	0.682	4.029	0.15	0.884	0.974	0.992
12 \rightarrow 3	0.109	0.747	4.084	0.148	0.891	0.978	0.993

1) *Influence on number of channels:* Table VIII and Table IX show the change in performance when varying the number of channels. In object detection, increasing the number of channels improves performance, likely due to the network encountering more diverse representations of TIR images. This

TABLE X: Sensitivity of the model to random D values.

Dataset: FLIR-ADAS				
Model: YOLO-X				
Compression	max mAP over 10 runs	min mAP over 10 runs	mean mAP over 10 runs	s.t.d. mAP over 10 runs
TE(3)	54.6	54.3	54.45	8.50×10^{-4}
TE(10)	52.2	52.5	52.36	9.66×10^{-4}
3 \rightarrow 3	54.8	54.5	54.57	9.49×10^{-4}
8 \rightarrow 3	55.5	55.3	55.42	7.89×10^{-4}
10 \rightarrow 3	55.8	53.9	54.53	7.8×10^{-4}
12 \rightarrow 3	56.0	55.6	55.85	1.35×10^{-4}

TABLE XI: FLOPs evaluation on TCNet-SparseRCNN

Num channels	Thermal Embedding Runtime (ms)	Sparse-RCNN FLOPs (FLOPs)	Extra FLOPs (FLOPs)
None	0	53.26G	0
TE(3)	4.35	53.26G	0
TE(10)	25.37	55.06G	1.8G
TC-3	4.35	53.27G	29.12M
TC-8	19.71	53.3G	77.66M
TC-10	25.37	53.31G	97.08M
TC-12	31.41	53.32G	116.5M

suggests that for semantic tasks like object detection, additional channels enhance the model’s robustness by introducing more variability in object appearances.

Conversely, for depth estimation, the best results are achieved with the original channel configuration. Although adding more channels reduces performance, the outcomes remain competitive with baseline models. This reduction in performance may stem from the decreased photometric consistency between consecutive frames that accompanies a higher number of channels, highlighting a task-specific trade-off in channel optimization.

2) *Sensitivity to random period values:* A crucial aspect of TCNet’s configuration is the selection of the temperature period D . While random sampling of D during training is viable, it raises concerns about potentially adverse effects on the performance during inference. To address this, we assessed the impact of random sampling by conducting ten iterations with randomly predefined seeds on TCNet and thermal embeddings trained with YOLOX, as shown in Table X. Interestingly, a higher number of channels yielded the lowest standard deviation 10^{-4} across iterations, showing reduced variability in performance. This suggests that randomness in D sampling does not detrimentally affect performance, but it rather mitigates the stochasticity associated with random D values, further demonstrating its efficacy in enhancing TCNet’s performance consistency.

3) *Computational Cost:* An important consideration when using TCNet is the increased computational cost. We analyzed the computational cost of Sparse-RCNN, the heaviest model, by measuring the Floating Point Operations per Second (FLOPs), as shown in Table XI. We denoted the runtime for thermal embedding measured on Intel i9-12900 CPU and noted the additional FLOPs incurred due to either adaptive channel compression or modifications to the convolutional backbone. Our analysis shows that increasing the number of channels for thermal embedding results in a linear rise in computational cost. However, employing adaptive channel compression adds only 0.1 GFLOPs while providing an 8.2%

gain in mAP. In contrast, using thermal embedding without adaptive compression adds 1.8 GFLOPs. Thus, adaptive channel compression not only improves performance but also is more efficient than solely using thermal embedding.

TABLE XII: Detection results for different augmentations

Augmentation	mAP	mAP @ 0.5	mAP @ 0.75	mAP @ small	mAP @ medium	mAP @ large
No Aug	0.379	0.63	0.397	0.311	0.528	0.586
HSV augmentation	0.362	0.583	0.401	0.271	0.552	0.617
Brightness jitter	0.369	0.585	0.408	0.29	0.553	0.618
Inversion	0.352	0.577	0.379	0.242	0.565	0.647
Gamma correction	0.35	0.559	0.389	0.261	0.558	0.641
Thermal Embedding	0.416	0.653	0.45	0.325	0.611	0.637
TCNet	0.457	0.705	0.498	0.361	0.675	0.627

4) *Comparison with other color augmentations:* As shown in Table XII, we compared thermal embedding with other commonly used color augmentations. For this, we trained Sparse-RCNN with augmentations applied to min-max TIR images. As the results demonstrate, thermal embedding induces performance improvement from simulating TIR images captured at diverse environments, surpasses other color augmentation methods. With adaptive channel compression (TCNet), we observe a further improvement in the performance.

V. CONCLUSION AND FUTURE WORKS

In this paper, we introduced Thermal Chameleon Network (TCNet), a task-adaptive tone-mapping framework for radiometric Thermal Infrared (TIR) images. TCNet’s capability to simulate unseen TIR environments through thermal embedding and adaptive channel compression has demonstrated robust performance in object detection and depth estimation.

However, TCNet currently relies on radiometric TIR images, limiting its applicability to non-radiometric datasets. Additionally, unlike the baselines, TCNet requires task and model specific training, necessitating separate models for different tasks. Future work should focus on adapting the thermal embedding for non-radiometric RAW TIR images and developing a more generalized version for broader use.

REFERENCES

- [1] Y.-S. Shin and A. Kim, “Sparse depth enhanced direct thermal-infrared slam beyond the visible spectrum,” *IEEE Robot. and Automat. Lett.*, vol. 4, no. 3, pp. 2918–2925, 2019.
- [2] U. Shin, K. Park, B.-U. Lee, K. Lee, and I. S. Kweon, “Self-supervised monocular depth estimation from thermal images via adversarial multi-spectral adaptation,” in *Proc. IEEE Winter Conf. on Applications of Comput. Vision.*, 2023, pp. 5798–5807.
- [3] F. Bao, X. Wang, S. H. Sureshbabu, G. Sreekumar, L. Yang, V. Aggarwal, V. N. Boddeti, and Z. Jacob, “Heat-assisted detection and ranging,” *Nature*, vol. 619, no. 7971, pp. 743–748, 2023.
- [4] S. Khattak, C. Papachristos, and K. Alexis, “Keyframe-based thermal-inertial odometry,” *J. of Field Robot.*, vol. 37, no. 4, pp. 552–579, 2020.
- [5] M. P. Das, L. Matthies, and S. Daftry, “Online photometric calibration of automatic gain thermal infrared cameras,” *IEEE Robot. and Automat. Lett.*, vol. 6, no. 2, pp. 2453–2460, 2021.
- [6] H. Gil, M.-H. Jeon, and A. Kim, “Fieldscale: Locality-aware field-based adaptive rescaling for thermal infrared image,” *IEEE Robot. and Automat. Lett.*, 2024.
- [7] U. Shin, K. Lee, B.-U. Lee, and I. S. Kweon, “Maximizing self-supervision from thermal image for effective self-supervised

- learning of depth and ego-motion,” *IEEE Robot. and Automat. Lett.*, vol. 7, no. 3, pp. 7771–7778, 2022.
- [8] A. Gödrich, D. König, G. Eilertsen, and M. Teutsch, “Joint tone mapping and denoising of thermal infrared images via multi-scale retinex and multi-task learning,” in *Infrared Tech. and Appli. XLIX*, vol. 12534. SPIE, 2023, pp. 275–291.
- [9] R. Xu, C. Chen, J. Peng, C. Li, Y. Huang, F. Song, Y. Yan, and Z. Xiong, “Toward raw object detection: A new benchmark and a new model,” in *Proc. IEEE Conf. on Comput. Vision and Pattern Recog.*, 2023, pp. 13 384–13 393.
- [10] U. Shin, K. Lee, S. Lee, and I. S. Kweon, “Self-supervised depth and ego-motion estimation for monocular thermal video using multi-spectral consistency loss,” *IEEE Robot. and Automat. Lett.*, vol. 7, no. 2, pp. 1103–1110, 2021.
- [11] C. Herrmann, M. Ruf, and J. Beyerer, “Cnn-based thermal infrared person detection by domain adaptation,” in *Autonomous Sys.: Sensors, Vehicles, Security, and the IoE*, vol. 10643. SPIE, 2018, pp. 38–43.
- [12] M. R. U. Saputra, P. P. De Gusmao, C. X. Lu, Y. Almalioglu, S. Rosa, C. Chen, J. Wahlström, W. Wang, A. Markham, and N. Trigoni, “Deeptio: A deep thermal-inertial odometry with visual hallucination,” *IEEE Robot. and Automat. Lett.*, vol. 5, no. 2, pp. 1672–1679, 2020.
- [13] M. M. Gündoğan, T. Aksoy, A. Temizel, and U. Halici, “Ir reasoner: Real-time infrared object detection by visual reasoning,” in *Proc. IEEE Conf. on Comput. Vision and Pattern Recog.*, 2023, pp. 422–430.
- [14] J. Veitch-Michaelis, “flirpy documentation,” <https://flirpy.readthedocs.io/en/latest/index.html>, 2023.
- [15] B. Mildenhall, P. Hedman, R. Martin-Brualla, P. P. Srinivasan, and J. T. Barron, “Nerf in the dark: High dynamic range view synthesis from noisy raw images,” in *Proc. IEEE Conf. on Comput. Vision and Pattern Recog.*, 2022, pp. 16 190–16 199.
- [16] T. FLIR, “Flir-adas v2,” <https://www.flir.com/oem/adas/adas-dataset-form/>, 2022.
- [17] A. J. Lee, Y. Cho, Y.-s. Shin, A. Kim, and H. Myung, “Vivid++: Vision for visibility dataset,” *IEEE Robot. and Automat. Lett.*, vol. 7, no. 3, pp. 6282–6289, 2022.
- [18] S. Yun, M. Jung, J. Kim, S. Jung, Y. Cho, M.-H. Jeon, G. Kim, and A. Kim, “Sthereo: Stereo thermal dataset for research in odometry and mapping,” in *Proc. IEEE/RSJ Intl. Conf. on Intell. Robots and Sys.* IEEE, 2022, pp. 3857–3864.
- [19] U. Shin, J. Park, and I. S. Kweon, “Deep depth estimation from thermal image,” in *Proc. IEEE Conf. on Comput. Vision and Pattern Recog.*, 2023, pp. 1043–1053.
- [20] T.-Y. Lin, P. Goyal, R. Girshick, K. He, and P. Dollár, “Focal loss for dense object detection,” in *Proc. IEEE Intl. Conf. on Comput. Vision*, 2017, pp. 2980–2988.
- [21] Z. Ge, S. Liu, F. Wang, Z. Li, and J. Sun, “Yolox: Exceeding yolo series in 2021,” *arXiv preprint arXiv:2107.08430*, 2021.
- [22] P. Sun, R. Zhang, Y. Jiang, T. Kong, C. Xu, W. Zhan, M. Tomizuka, L. Li, Z. Yuan, C. Wang *et al.*, “Sparse r-cnn: End-to-end object detection with learnable proposals,” in *Proc. IEEE Conf. on Comput. Vision and Pattern Recog.*, 2021, pp. 14 454–14 463.
- [23] A. Radford, J. W. Kim, C. Hallacy, A. Ramesh, G. Goh, S. Agarwal, G. Sastry, A. Askell, P. Mishkin, J. Clark *et al.*, “Learning transferable visual models from natural language supervision,” in *Proc. Intl. Conf. on Machine Learning*. PMLR, 2021, pp. 8748–8763.
- [24] R. Girdhar, A. El-Nouby, Z. Liu, M. Singh, K. V. Alwala, A. Joulin, and I. Misra, “Imagebind: One embedding space to bind them all,” in *Proc. IEEE Conf. on Comput. Vision and Pattern Recog.*, 2023, pp. 15 180–15 190.